

Twin branching in shape memory alloys: a 1D continuum model with energy dissipation effects

Stanisław Stupkiewicz^{a,*}, Seyedshoja Amini^a, Mohsen Rezaee-Hajidehi^a

^a*Institute of Fundamental Technological Research, Polish Academy of Sciences,
Pawińskiego 5B, 02-106 Warsaw, Poland.*

Abstract

We develop a 1D continuum model of twin branching in shape memory alloys. The free energy of the branched microstructure comprises the interfacial and elastic strain energy contributions, both expressed in terms of the average twin spacing treated as a continuous function of the position. The total free energy is then minimized, and the corresponding Euler–Lagrange equation is solved numerically using the finite element method. The model can be considered as a continuum counterpart of the recent discrete model of Seiner et al. (2020), and our results show a very good agreement with that model in the entire range of physically relevant parameters. Furthermore, our continuum setting facilitates incorporation of energy dissipation into the model. The effect of rate-independent dissipation on the evolution of the branched microstructure is thus studied. The results show that significant effects on the microstructure and energy of the system are expected only for relatively small domain sizes.

Keywords: Microstructure evolution, Martensite, Twinning, Interfaces, Energy dissipation

1. Introduction

Martensitic transformation, which is the basic deformation mechanism in shape memory alloys, proceeds through formation and evolution of microstructure (Bhattacharya, 2003). Interfaces between the product phase (martensite) and the parent phase (austenite) constitute the most common element of the microstructure. Kinematic compatibility of the two phases at such interfaces is typically achieved through twinning of martensite so that martensite appears in the form of a laminate of two twin-related variants. Twin branching, which is the subject of this work, is a phenomenon frequently observed in experiments (e.g., Chu, 1993; Bronstein et al., 2019; Qin et al., 2023) in which the thickness of the individual twins is gradually reduced towards the austenite–martensite interface.

The phenomenon of twin branching can be explained by the propensity of the material to minimize its total free energy which includes the interfacial energy of twin boundaries and the energy of elastic strains that accommodate the local incompatibility of the phases at the austenite–martensite interface. The latter energy is reduced when the twin spacing is decreased (close to the austenite–martensite interface), while the former energy is reduced when the twin spacing is increased (far

*Corresponding author

Email addresses: sstupkie@ipt.pan.pl (Stanisław Stupkiewicz), samini@ipt.pan.pl (Seyedshoja Amini), mrezaee@ipt.pan.pl (Mohsen Rezaee-Hajidehi)

from the austenite–martensite interface). Accordingly, the total energy can be minimized by a microstructure with the twin spacing varying as a function of the distance from the austenite–martensite interface, and this is achieved through twin branching. Note that branching itself incurs an energetic cost that participates in the competition between the free energy contributions.

Twin branching is related, through the energy-minimization background and sometimes also through the appearance, to other phenomena observed in natural and engineered materials. These include branching in magnetic domains (Hubert and Schäfer, 1998), magnetic flux structures in superconductors (Huebener, 2001), hierarchical wrinkling patterns in thin films (Vandeparre et al., 2010; Ma et al., 2020), and others.

The theoretical analysis of twin branching started with the seminal contributions of Kohn and Müller (1992, 1994), followed by many related works, mostly in the mathematics community (e.g., Capella and Otto, 2009; Conti, 2000; Chan and Conti, 2015; Dondl et al., 2016; Simon, 2021). This line of research delivers, in particular, the scaling laws for energy and for characteristic dimensions of the branched microstructure. As a follow up, a quantitative model of twin branching in shape memory alloys has been recently developed by Seiner et al. (2020). The model assumes that the branched microstructure consists of a family of self-similar branching generations, as in several earlier models, and refined estimates of the elastic strain energy of branching have been derived for the considered microstructure. The parameters characterizing the actual microstructure are then obtained by minimizing the total free energy. This model will be used as a reference for our model developed below.

Direct spatially-resolved simulation of a branched microstructure by using, for example, the phase-field method, is not feasible because of the multiscale nature of the branched microstructure. However, some features characteristic for twin branching can be observed in phase-field simulations (e.g., Finel et al., 2010; Tůma and Stupkiewicz, 2016; Amini et al., 2023). These are limited to tip splitting of martensite needles, or the like, and thus correspond to just a single branching generation. To the best of our knowledge, spatially-resolved simulations of hierarchical branched microstructures have not been reported to date. A kind of hierarchical twin branching is reported in the related work of Li and Luskin (1999), but the interfacial energy is not included in that model (only the elastic strain energy is minimized) so that the model does not capture the essential competition between the interfacial and elastic strain energy contributions.

In this paper, we propose a new approach to the modeling of twin branching: a continuum 1D model is developed in which the twin spacing is treated as a continuous function of the position. In this continuum setting, the free energy of the system is formulated which includes three contributions: the interfacial energy of twin boundaries, the elastic strain energy of branching, and the energy of elastic strains that accommodate the local incompatibility at the austenite–twinned martensite interface. The total free energy is then minimized, thus delivering the governing equation (ODE) for the twin spacing that is solved numerically using the finite element method. The model can be considered a continuum counterpart of the discrete model of Seiner et al. (2020), and we show that the predictions of the two models agree very well for a wide range of model parameters.

Secondly, for the first time, we consider the energy dissipation associated with the evolution of the branched microstructure. This is facilitated by our continuum formulation, as development of the respective discrete formulation would be difficult, if possible at all. The evolution equation for

the twin spacing is obtained by minimization of the rate potential that comprises the rate of the total free energy and the rate-independent dissipation potential. Finite-element computations are then carried out for a high but realistic value of the rate-independent threshold for propagation of twin interfaces. The results suggest that the energy dissipation effects are small or even negligible in most cases. Only for a relatively high value of the dimensionless interfacial energy (which corresponds, for instance, to a small size of the twinned domain) and for a high interface propagation threshold, a significant effect on both the microstructure (twin spacing) and energy can be observed.

The remainder of the paper is organized as follows. In Section 2, the discrete model of twin branching of Seiner et al. (2020) is briefly outlined as a reference for our subsequent developments. In Section 3, the continuum model of twin branching is developed and sample results are presented, including a comparison with the predictions of the model of Seiner et al. (2020). In Section 4, energy dissipation is introduced into the model and the corresponding effects are studied for a few representative cases of evolution of the branched microstructure. Technical details concerning the derivation of the evolution problem and its computational treatment are presented in appendices. A general discussion on the model and its applicability is presented in Section 5, followed by the Conclusion in Section 6.

2. Background

2.1. Austenite–twinned martensite interface

In majority of shape memory alloys, the interface between the austenite and the martensite forms such that the martensite is internally twinned, i.e., it has the form of a fine laminate of two twin-related variants of martensite. This is because a single martensite variant is usually not compatible with the austenite and thus cannot form a low-energy (stress-free) austenite–martensite interface (Bhattacharya, 2003). The orientation and other features of the austenite–twinned martensite (A–MM) interface can be predicted by using the crystallographic theory of martensite (Ball and James, 1987; Bhattacharya, 2003), which relies on the kinematic compatibility conditions formulated for the twin interfaces and for the A–MM interface.

Consider thus two variants of martensite characterized by the transformation stretch tensors \mathbf{U}_A and \mathbf{U}_B . In stress-free conditions, the condition of kinematic compatibility of the two variants along a planar interface of the unit normal \mathbf{n} can be written in the form of the following *twinning equation*,

$$\mathbf{R}\mathbf{U}_A - \mathbf{U}_B = \hat{\mathbf{a}} \otimes \mathbf{n}, \quad (1)$$

where $\hat{\mathbf{a}}$ is a non-zero vector and \mathbf{R} is a rotation tensor. Consider further a simple laminate formed by the two martensite variants with λ denoting the volume fraction of the variant \mathbf{U}_A . The *overall* compatibility of the austenite and twin laminate has then the form of the *habit plane equation*,

$$\mathbf{Q}(\lambda\mathbf{R}\mathbf{U}_A + (1 - \lambda)\mathbf{U}_B) - \mathbf{I} = \mathbf{b} \otimes \mathbf{m}, \quad (2)$$

where \mathbf{m} is the unit normal to the (planar) A–MM interface, \mathbf{b} is a non-zero vector, \mathbf{Q} is a rotation tensor, and \mathbf{I} is the unit tensor that corresponds to the deformation gradient of the unstressed austenite. The unknown \mathbf{R} , $\hat{\mathbf{a}}$, \mathbf{n} , \mathbf{Q} , \mathbf{b} , \mathbf{m} , and λ can be found using the procedure described, for instance, in Bhattacharya (2003).

It is stressed that the habit plane equation (2) describes the overall compatibility between the twin laminate and the austenite, while the individual variants of martensite are not compatible with the austenite. Accordingly, elastic strains are needed to accommodate the corresponding local incompatibility, hence a transition layer with non-zero elastic strains necessarily forms along the A-MM interface. The energy of the transition layer depends on the characteristic spacing of the twin laminate (twin spacing) and is, to the first order, proportional to it. This energy can thus be lowered by reducing the twin spacing. However, a finely twinned laminate would have a high density of twin interfaces and thus a high total energy of twin boundaries, since each twin interface has a non-zero energy proportional to the area of the interface. The actual twin spacing minimizing the total energy would thus result from the competition between the elastic micro-strain energy in the transition layer and the total interfacial energy of twin boundaries (Khachaturyan, 1983). The total energy can be further minimized through formation of a branched microstructure such that twins are (relatively) coarse far from the A-MM interface to reduce the interfacial energy and are fine close to the A-MM interface to reduce the elastic micro-strain energy. The branching itself is associated with the energy of elastic strains needed to accommodate the incompatibility induced by the deviation from the fully compatible twin interfaces, and this energy also contributes to the total energy balance.

2.2. Discrete model of twin branching

A discrete model of twin branching has been recently developed by Seiner et al. (2020), and this model is briefly summarized below. The model is based on the minimization of the total free energy of the specific branching microstructure shown in Fig. 1(a). It is assumed that the twin spacing is refined through a sequence of self-similar branching segments. Each branching generation, indexed by i , is formed by a layer of the corresponding unit cells (segments) that are repeated in a periodic manner with L_i denoting the length measured in the direction perpendicular to the A-MM interface and h_i denoting the twin spacing measured along the A-MM interface, while the width of the segment is equal to $2h_i$, see Fig. 1(b). Here and in the following, we keep the notation used by Seiner et al. (2020), except that the twin spacing is denoted by h_i rather than by d_i . Note that the first layer of the length L_0 and spacing h_0 is not branched, see Fig. 1(a).

For a given total length L of the twinned domain, the microstructure of the branched twin laminate is characterized by the number of branching generations N , the twin spacing h_0 in the first layer, and the individual lengths L_i . These variables are determined by minimizing the total free energy E ,

$$E = \frac{1}{h_0} \left(E_{\text{surf}}^{(0)} + \sum_{i=1}^N 2^{i-1} (E_{\text{elast}}^{(i)} + E_{\text{surf}}^{(i)}) \right) + \Gamma h_N \rightarrow \min, \quad (3)$$

where $E_{\text{elast}}^{(i)}$ denotes the elastic strain energy of one segment in the i -th branching layer, $E_{\text{surf}}^{(i)}$ denotes the interfacial energy of the twin boundaries contained within that segment, and the lengths L_i must satisfy the constraint $L = \sum_{i=0}^N L_i$. The last term represents the elastic micro-strain energy in the transition layer along the A-MM interface with Γ denoting the energy factor and $h_N = h_0/2^N$ denoting the twin spacing at the A-MM interface. Considering that the first layer ($i = 0$) is not branched, the corresponding elastic strain energy is equal to zero, $E_{\text{elast}}^{(0)} = 0$.

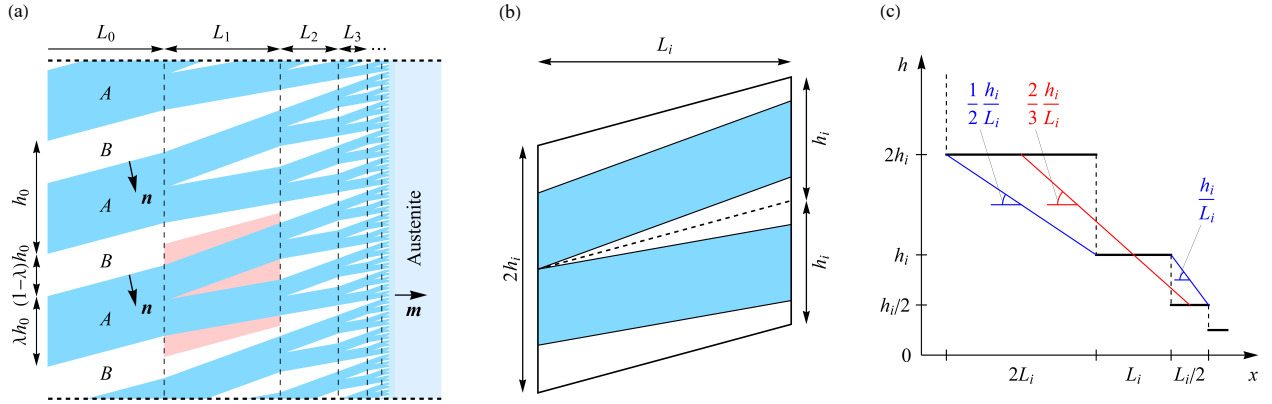


Figure 1: Discrete model of twin branching (Seiner et al., 2020): (a) self-similar microstructure with N branching generations; (b) unit cell; (c) twin spacing h as a function of the position x . Possible ways to determine the derivative of a continuous function $h(x)$ are shown in panel (c).

For the microstructure of the branching segment shown in Fig. 1(b), an upper-bound estimate of the elastic strain energy of branching has been developed in the following form, see Eq. (S.6) in the supplementary material of Seiner et al. (2020),

$$E_{\text{elast}}^{(i)} = \frac{1}{4} \mu \lambda (1 - \lambda) g_2 L_i h_i \varepsilon_i^2, \quad \varepsilon_i = \frac{(1 - \lambda) \alpha h_i}{L_i}, \quad (4)$$

where

$$\alpha = \sqrt{1 - (\mathbf{m} \cdot \mathbf{n})^2}, \quad g_2 = \frac{1}{2} (|\mathbf{a}|^2 + (\mathbf{a} \cdot \mathbf{m})^2), \quad (5)$$

and μ denotes the shear modulus. Here, λ , \mathbf{m} , \mathbf{n} , and $\mathbf{a} = \mathbf{Q}\hat{\mathbf{a}}$ follow from the crystallographic theory outlined in Section 2.1. The above estimate corresponds to the case of elastic isotropy. A more refined estimate considering elastic anisotropy is given by Eq. (30) in Seiner et al. (2020). The energy $E_{\text{elast}}^{(i)}$ refers to a unit length in the out-of-plane direction, and the density per unit volume is thus obtained by dividing $E_{\text{elast}}^{(i)}$ by the area of the segment,

$$\frac{E_{\text{elast}}^{(i)}}{2h_i L_i} = \frac{1}{8} \mu \lambda (1 - \lambda)^3 \alpha^2 g_2 \left(\frac{h_i}{L_i} \right)^2. \quad (6)$$

This result will be used to calibrate our continuum model in Section 3.

Assuming that $L_i \gg h_i$, the interfacial energy $E_{\text{surf}}^{(i)}$ of branched segments ($i \geq 1$) and its density can be simply estimated as

$$E_{\text{surf}}^{(i)} = \frac{4L_i \gamma}{\alpha}, \quad \frac{E_{\text{surf}}^{(i)}}{2h_i L_i} = \frac{2\gamma}{\alpha h_i}, \quad (7)$$

where γ denotes the interfacial energy of twin boundaries (density per unit area), a material parameter that is assumed constant, i.e., independent on the interface orientation. Note that the nominal twinning planes (of normal \mathbf{n}) are not necessarily perpendicular to the A-MM interface (of normal \mathbf{m}), see Fig. 1, hence the factor α in Eq. (7), see also Eq. (5)₁. Since there are two twin interfaces in each segment of the first layer ($i = 0$), we have $E_{\text{surf}}^{(0)} = 2L_0 \gamma / \alpha$. The actual estimate of $E_{\text{surf}}^{(i)}$ used in the model of Seiner et al. (2020) includes additional correction terms that account for the deviation of the interface orientation from the theoretical one and for the different lengths of the

individual interfaces within the segment. However, in our model, we will only consider the simple estimate in Eq. (7).

The elastic micro-strain energy factor Γ in Eq. (3), for which Seiner et al. (2020) developed a separate construction and derived the corresponding upper-bound estimate of the elastic strain energy, is discussed later.

3. Continuum model of twin branching

3.1. Twin spacing as a continuous function

In our continuum model, the twin spacing h is considered to be a continuous function of the position x , thus $h = h(x)$ for $0 \leq x \leq L$. Considering that real microstructures do not exhibit periodicity nor perfect arrangement of branching generations, as assumed in the discrete model of Seiner et al. (2020), the twin spacing $h(x)$ should be interpreted as the average spacing measured over a representative part of the A–MM interface and determined at a given distance from it. Note that, in accord with Seiner et al. (2020), the twin spacing $h(x)$ is here measured in the direction parallel to the A–MM interface, and the spatial coordinate x is measured in the direction perpendicular to the A–MM interface with $x = 0$ at the free boundary and $x = L$ at the A–MM interface, see Fig. 1(a).

The estimate of the elastic strain energy of branching, Eq. (4), will be used to characterize the elastic strain energy in the continuum setting. To this end, we note that the energy density within a single cell depends on the ratio h_i/L_i , see Eq. (6). Now, referring to Fig. 1(c), the spatial derivative of $h(x)$ can be related to the ratio h_i/L_i through

$$h_{,x} = \frac{dh}{dx} \approx \frac{\Delta h}{\Delta x} \approx \frac{\frac{1}{2}h_i - 2h_i}{\frac{1}{4}L_i + 2L_i} = -\frac{2h_i}{3L_i}. \quad (8)$$

By combining Eqs. (6) and (8), the elastic strain energy density can thus be expressed as a function of the (squared) spatial derivative $h_{,x}$ of the twin spacing h ,

$$\frac{E_{\text{elast}}^{(i)}}{2h_iL_i} = \frac{1}{2}A(h_{,x})^2, \quad A = \frac{9}{16}\mu\lambda(1-\lambda)^3\alpha^2g_2, \quad (9)$$

and this estimate will be used in our continuum model.

Note that the factor $\frac{2}{3}$ in Eq. (8) results from the specific construction adopted here, see Fig. 1(c), and is considered a reasonable estimate. However, factors other than $\frac{2}{3}$ could be adopted in the range between $\frac{1}{2}$ and 1, as also illustrated in Fig. 1(c).

3.2. Governing equations

The governing equations of the continuum model will now be derived through minimization of the total free energy of the system. The free energy density (per unit volume of the branched microstructure) is formulated in the following form,

$$\phi(h, h_{,x}) = \frac{1}{2}A(h_{,x})^2 + \frac{2\gamma}{\alpha h}. \quad (10)$$

The first term is the elastic strain energy contribution derived above, see Eq. (9). The second term describes the interfacial energy of twin boundaries and is a continuum counterpart of Eq. (7)₂. The

free energy function ϕ is the density per unit volume, i.e., the density per unit area of the A–MM interface and per unit length along the x -axis.

The total free energy functional (density per unit area of the A–MM interface) is now obtained by integrating the free energy density ϕ over the length of the domain,

$$\Phi = \int_0^L \phi(h, h_{,x}) dx + \Gamma h|_{x=L}. \quad (11)$$

The total free energy includes also the energy of elastic micro-strains at the A–MM interface, which is introduced by the second term in Eq. (11). It can be shown that this energy is proportional to the twin spacing at $x = L$, denoted by $h|_{x=L}$, as indicated in Eq. (11), and Γ is the corresponding proportionality factor. Seiner et al. (2020) have developed a separate construction to estimate Γ , see their Fig. 7(b). An alternative approach is to estimate Γ by solving an adequate boundary value problem combined with shape optimization, which can be performed using either a sharp-interface framework (Maciejewski et al., 2005; Stupkiewicz et al., 2007) or a diffuse-interface framework within the phase-field method (Tůma and Stupkiewicz, 2016; Amini et al., 2023). Below, we adopt the value of Γ by referring to the results of phase-field simulations, as discussed in Section 3.4.

The total free energy Φ involves four parameters, namely γ , A , α , and Γ , and the size L of the branched domain. The twin boundary energy γ is a material parameter. Parameters A , α , and Γ depend on the specific A–MM microstructure. Moreover, A and Γ depend on the elastic properties of the phases.

Let us assume that the microstructure of the branched martensite domain is formed such that the total free energy is minimized. This is a common approach in the modeling of martensitic microstructures, followed in particular in the crystallographic theory of martensite (Ball and James, 1987; Bhattacharya, 2003), as well as in the modeling of twin branching (Kohn and Müller, 1992; Seiner et al., 2020). This assumption will be relaxed in Section 4 where the evolution of the microstructure will be considered and the associated energy dissipation will be accounted for. The twin spacing $h(x)$ is thus found by minimizing the total free energy Φ ,

$$\Phi \rightarrow \min_h. \quad (12)$$

The necessary condition for the minimum of Φ , i.e. the condition of stationarity of Φ with respect to an arbitrary variation δh of h , reads

$$0 = \delta_h \Phi = \int_0^L \left(Ah_{,x} \delta h_{,x} - \frac{2\gamma}{\alpha h^2} \delta h \right) dx + \Gamma \delta h|_{x=L} \quad \forall \delta h. \quad (13)$$

The local (strong) form of the governing equation can then be obtained in a standard manner. Using the divergence theorem, Eq. (13) is transformed to

$$\int_0^L \left(-Ah_{,xx} - \frac{2\gamma}{\alpha h^2} \right) \delta h dx - Ah_{,x} \delta h|_{x=0} + (Ah_{,x} + \Gamma) \delta h|_{x=L} = 0 \quad \forall \delta h, \quad (14)$$

where the whole second term (i.e., both $h_{,x}$ and δh) is evaluated at $x = 0$ (this is denoted by the vertical bar with a subscript), and likewise the whole third term is evaluated at $x = L$. Following the standard argument, Eq. (14) implies the following local form of the governing equation,

$$h_{,xx} + \frac{2\gamma}{\alpha Ah^2} = 0 \quad \text{for } x \in [0, L] \quad (15)$$

along with the boundary conditions

$$h_{,x}|_{x=0} = 0, \quad h_{,x}|_{x=L} = -\frac{\Gamma}{A}. \quad (16)$$

Note that the boundary condition at $x = 0$, Eq. (16)₁, is the continuum counterpart of the non-branched first segment in the construction proposed by Seiner et al. (2020), see Fig. 1(a).

Introducing dimensionless twin spacing \bar{h} and dimensionless coordinate \bar{x} , both normalized using L ,

$$\bar{h} = \frac{h}{L}, \quad \bar{x} = \frac{x}{L}, \quad (17)$$

Eqs. (15) and (16) can be written in a dimensionless form, i.e.,

$$\bar{h}_{,\bar{x}\bar{x}} + \frac{2\bar{\gamma}}{\bar{h}^2} = 0 \quad \text{for } \bar{x} \in [0, 1], \quad \bar{h}_{,\bar{x}}|_{\bar{x}=0} = 0, \quad \bar{h}_{,\bar{x}}|_{\bar{x}=1} = -\bar{\Gamma}. \quad (18)$$

Accordingly, the model involves two dimensionless material parameters,

$$\bar{\gamma} = \frac{\gamma}{\alpha AL}, \quad \bar{\Gamma} = \frac{\Gamma}{A}. \quad (19)$$

For future use, let us also introduce dimensionless free energy density $\bar{\phi}$ and dimensionless total free energy $\bar{\Phi}$,

$$\bar{\phi} = \frac{\phi}{A} = \frac{1}{2}(\bar{h}_{,\bar{x}})^2 + \frac{2\bar{\gamma}}{\bar{h}}, \quad \bar{\Phi} = \frac{\Phi}{AL} = \int_0^1 \bar{\phi}(\bar{h}, \bar{h}_{,\bar{x}}) d\bar{x} + \bar{\Gamma} \bar{h}|_{\bar{x}=1}. \quad (20)$$

The dimensionless counterpart of the weak form (13) reads

$$\int_0^1 \left(\bar{h}_{,\bar{x}} \delta \bar{h}_{,\bar{x}} - \frac{2\bar{\gamma}}{\bar{h}^2} \delta \bar{h} \right) d\bar{x} + \bar{\Gamma} \delta \bar{h}|_{\bar{x}=1} = 0 \quad \forall \delta \bar{h}. \quad (21)$$

The above weak form will be used as a basis for an approximate solution of the problem using the finite element method.

3.3. Finite-element treatment

While the weak form (13) and its dimensionless counterpart (21) are fully equivalent, the latter appears to be more convenient in computational practice, as follows from our preliminary simulations. The finite-element solution is thus obtained by introducing a standard piecewise-linear approximation of the dimensionless twin spacing \bar{h} over the interval $[0, 1]$. Application of the Galerkin method delivers then a set of nonlinear equations that are solved using the Newton method. Note that an adequate initialization of the iterative scheme is needed to avoid division by zero in view of the term \bar{h}^2 in the denominator in the weak form (21). Further, the nodal (Lobatto) integration is employed, since convergence problems or non-physical solutions with $\bar{h} < 0$ are often encountered in the case of the Gauss integration. Standard details of the finite-element treatment are omitted here.

Considering that the actual solutions may be characterized by a high gradient in the vicinity of $\bar{x} = 1$, see e.g. Fig. 2(a) below, the finite-element mesh is significantly refined towards $\bar{x} = 1$. As a result, highly accurate solutions can be obtained in most cases for the number of elements of the order of 100. However, in the most demanding cases ($\bar{\gamma} < 10^{-6}$), a much finer mesh of 10^4 elements is needed to obtain a converged solution.

3.4. Model predictions

Sample results are shown in Fig. 2 in order to illustrate the predictions delivered by the model. The material parameters correspond to those adopted by Seiner et al. (2020) for the CuAlNi alloy, and the same specific A–MM microstructure is considered. Specifically, the twin boundary energy is adopted as $\gamma = 0.1 \text{ J/m}^2$, and parameter A characterizing the elastic strain energy of branching is computed according to Eq. (9)₂ using $\mu = 70 \text{ GPa}$, $\lambda = 0.6992$, $g_2 = 0.03648$, and $\alpha = 0.5642$, so that $A = 8.7 \text{ MJ/m}^3$.

The elastic micro-strain energy factor Γ is adopted based on the results of the micromechanical analysis carried out using the phase-field method (Tůma and Stupkiewicz, 2016). Out of the four crystallographically distinct microstructures of the A–MM interface, the one considered by Seiner et al. (2020) corresponds to microstructure M3 in the notation used by Tůma and Stupkiewicz (2016). The corresponding values of the energy factor Γ_{am}^e reported in Fig. 10 in Tůma and Stupkiewicz (2016) range from about 2 MJ/m^3 to 5 MJ/m^3 depending on the twin spacing and interface thickness parameter of the phase-field model. The lower values of Γ_{am}^e are associated with a local branching mechanism that becomes effective when the twin spacing is greater than 30 nm , see Fig. 6 in Tůma and Stupkiewicz (2016), and also with a greater interface thickness in the phase-field model. Therefore, we adopt the value of $\Gamma_{\text{am}}^e \approx 5 \text{ MJ/m}^3$ as a reasonable estimate, which is also consistent with the results of the sharp-interface modeling reported by Stupkiewicz et al. (2007). Note that the factor Γ_{am}^e in Tůma and Stupkiewicz (2016) corresponds to the twin spacing measured in the direction normal to the twin interfaces, while the factor Γ in Eq. (11) corresponds to the twin spacing measured along the A–MM interface. Accordingly, we have $\Gamma = \alpha \Gamma_{\text{am}}^e$, and thus the value of $\Gamma = 3 \text{ MJ/m}^3$ will be used in the following. The corresponding dimensionless parameter is equal to $\bar{\Gamma} = 0.345$, see Eq. (19)₂.

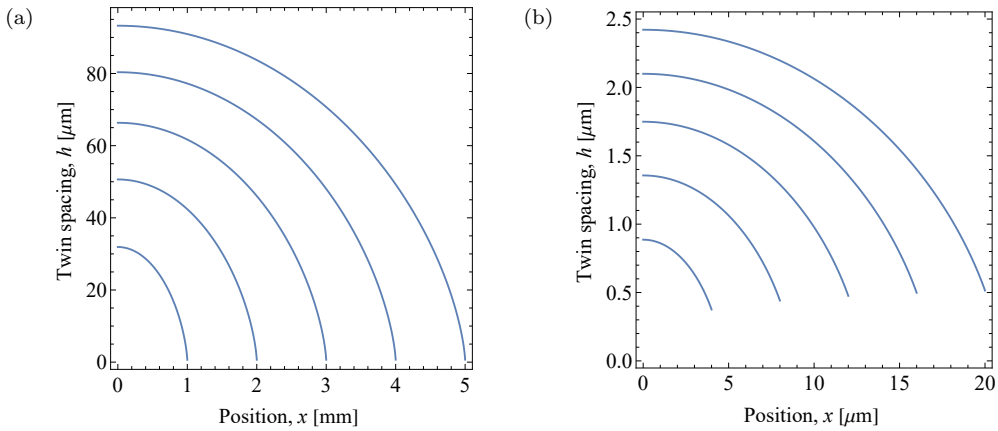


Figure 2: Twin spacing $h(x)$ for (a) relatively large domain with L varied between 1 mm ($\bar{\gamma} = 2 \times 10^{-5}$) and 5 mm ($\bar{\gamma} = 4 \times 10^{-6}$) and (b) relatively small domain with L varied between $4 \mu\text{m}$ ($\bar{\gamma} = 5 \times 10^{-3}$) and $20 \mu\text{m}$ ($\bar{\gamma} = 10^{-3}$).

Finally, two ranges of the size L of the twinned martensite domain are considered. The first range corresponds to a relatively large domain with L varied between 1 mm and 5 mm , where the latter value was used in the main illustrating example of Seiner et al. (2020), see their Fig. 8. The respective results are shown in Fig. 2(a). The second range corresponds to a relatively small domain

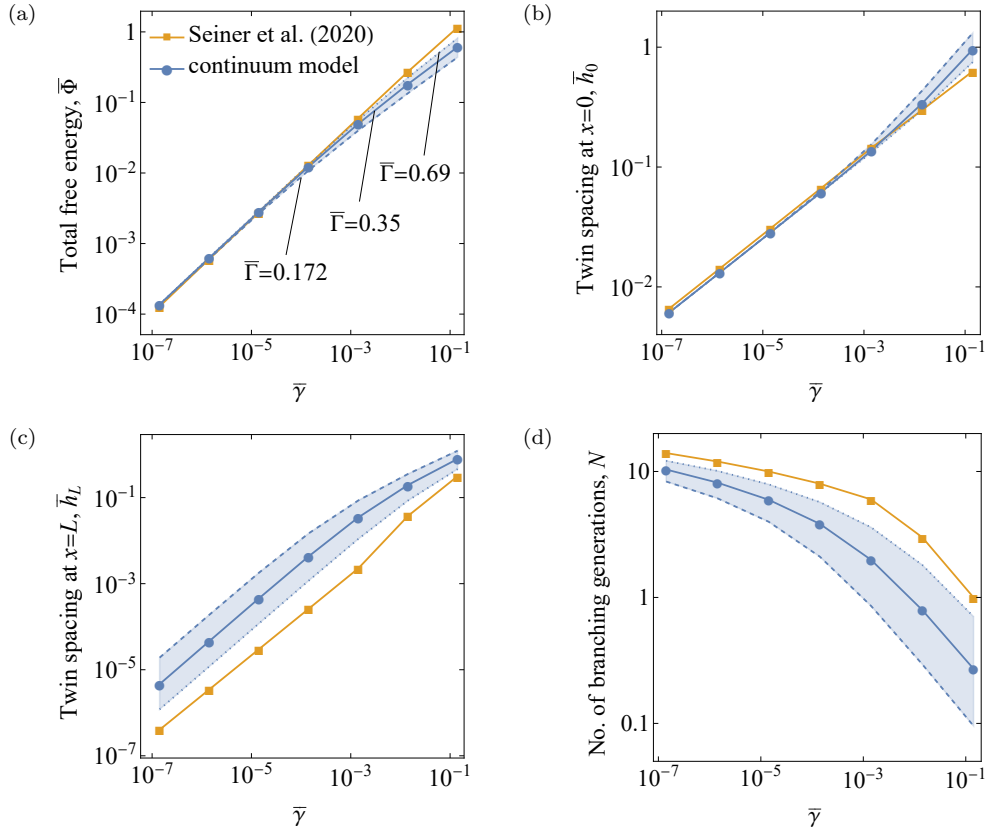


Figure 3: Predictions of the present continuum model compared to those of the discrete model of Seiner et al. (2020): (a) dimensionless total free energy $\bar{\Phi}$, (b) dimensionless twin spacing \bar{h}_0 at $x = 0$, (c) dimensionless twin spacing \bar{h}_L at $x = L$, and (d) the number of branching generations N ; all as a function of the dimensionless twin boundary energy $\bar{\gamma}$, see Eq. (19)₁. The shaded regions indicate the range of values corresponding to $\bar{\Gamma}$ decreased twice (dashed lines) and increased twice (dotted lines).

with L varied between $4 \mu\text{m}$ and $20 \mu\text{m}$, and the respective results are shown in Fig. 2(b). It can be seen that twin branching and the corresponding refinement of the microstructure towards the A–MM interface is more pronounced for larger domains.

Fig. 3 presents a comprehensive comparison of the predictions of the present continuum model with those of the discrete model of Seiner et al. (2020), as reported in their Table 1. The latter results have been reported for the length L varied between 10^4 nm and 10^7 nm (four values) and for the material length γ/μ varied between 10^{-4} nm and 10^{-1} nm (four values). Apparently, the 16 cases reported by Seiner et al. (2020) collapse with a very good accuracy to seven distinct cases in our dimensionless representation, Eqs. (17), (19) and (20), with the dimensionless twin boundary energy $\bar{\gamma}$ spanning six decades from about 10^{-7} to 10^{-1} .

Fig. 3 shows a very good agreement of the two models over the whole range of $\bar{\gamma}$. In particular, an almost perfect agreement is demonstrated in terms of the dimensionless total free energy $\bar{\Phi}$ and twin spacing \bar{h}_0 at the free end ($x = 0$), see Fig. 3(a,b), except for a small deviation observed for the largest values of $\bar{\gamma}$ (to be commented below). The agreement in terms of \bar{h}_L , the dimensionless twin spacing at the A–MM interface (at $x = L$), is somewhat worse, see Fig. 3(c). Still it can be

considered acceptable, the more that it does not affect the good agreement in the total energy $\bar{\Phi}$ and in the twin spacing \bar{h}_0 .

Fig. 3(d) compares the number of branching generations N . In the discrete model of Seiner et al. (2020), N is a positive integer such that $h_L = h_N = h_0/2^N$. In the case of our continuum model, N is defined as

$$N = \log_2 \left(\frac{h_0}{h_L} \right), \quad (22)$$

and, clearly, takes non-integer values. Consistent with the case of \bar{h}_L in Fig. 3(c), a visible difference between the two models is observed also in the case of N , however, both models follow the same trend.

For $\bar{\gamma} = 10^{-1}$ (the largest value of $\bar{\gamma}$ considered), the continuum model predicts $N = 0.27$, with the interpretation that only a fraction of twin lamellae would branch. The discrete model predicts then one branching generation, $N = 1$. This may justify the (small) deviation of the two models in terms of $\bar{\Phi}$ and \bar{h}_0 observed for the largest values of $\bar{\gamma}$, see Fig. 3(a,b). Indeed, when the number of branching generations is small, it is natural to expect that a piecewise constant distribution of twin spacing and a continuous distribution yield somewhat different results. Actually, it may be surprising that the agreement is then still rather good. Note that, adopting the values of parameters γ , A , and α as specified above for the CuAlNi alloy, the case of $\bar{\gamma} = 10^{-1}$ would correspond to $L = 0.2 \mu\text{m}$, which is a very small and thus non-physical value.

Fig. 3 illustrates also the sensitivity of the model predictions to the value of the elastic micro-strain energy factor Γ . The shaded regions in each diagram indicate the range of values that correspond to parameter $\bar{\Gamma}$ decreased twice and increased twice with respect to the reference value of $\bar{\Gamma} = 0.345$. It can be seen that the total energy $\bar{\Phi}$ and the twin spacing \bar{h}_0 are practically insensitive to $\bar{\Gamma}$ over a wide range of values of $\bar{\gamma}$, and only for the largest values of $\bar{\gamma}$ they show a moderate sensitivity to $\bar{\Gamma}$. It can also be seen that the agreement with the discrete model is significantly improved for $\bar{\Gamma} = 0.690$ (the dotted curves), and even a better, almost perfect agreement would be achieved for $\bar{\Gamma}$ increased further, say, to $\bar{\Gamma} = 1$.

Fig. 4 showcases the individual contributions Φ_i to the total free energy Φ as a function of $\bar{\gamma}$, where

$$\Phi_{\text{el}} = \int_0^L \frac{1}{2} A(h,x)^2 dx, \quad \Phi_{\text{int}} = \int_0^L \frac{2\gamma}{\alpha h} dx, \quad \Phi_{\Gamma} = \Gamma h|_{x=L}, \quad (23)$$

see Eqs. (10) and (11). The interfacial energy contribution Φ_{int} constitutes the largest fraction of Φ over the entire range of $\bar{\gamma}$. The contribution of the elastic strain energy, Φ_{el} , amounts to about one third of Φ for small $\bar{\gamma}$ and decreases towards zero for $\bar{\gamma} = 10^{-1}$. This naturally correlates with the intensity of twin branching characterized by N , see Fig. 3(d). Finally, the contribution of the elastic micro-strain energy at the A-MM interface, Φ_{Γ} , is negligible for $\bar{\gamma} = 10^{-7}$ and reaches nearly 50% for $\bar{\gamma} = 10^{-1}$. In this latter regime, where $\bar{\gamma}$ is large and N tends to zero (no branching), the two contributions Φ_{int} and Φ_{Γ} tend to be equal. Equality of the two contributions is a result that is consistent with a simple model minimizing the total interfacial energy of a twinned plate in the absence of twin branching (Petryk et al., 2006, 2010).

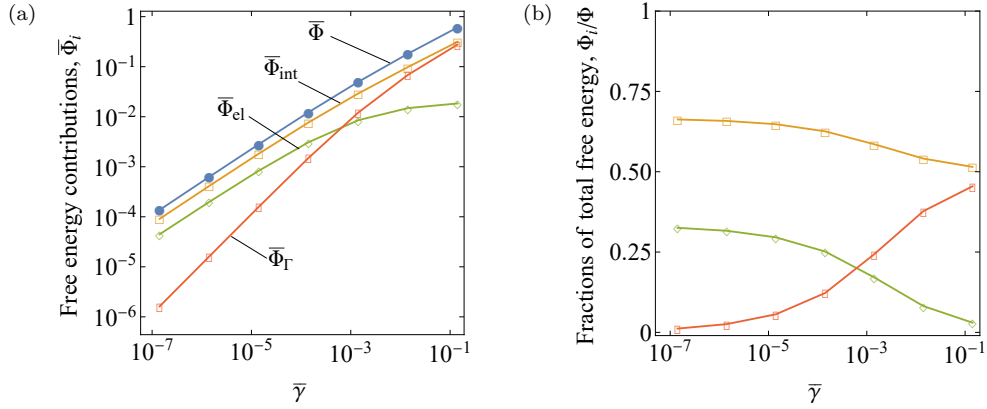


Figure 4: Individual contributions to the total free energy Φ as a function of $\bar{\gamma}$: (a) dimensionless energy contributions $\bar{\Phi}_i$; (b) fractions Φ_i/Φ .

4. Introducing dissipation effects

4.1. Overall dissipation potential

Evolution of the branched microstructure is associated with propagation of twin interfaces, and this propagation is now considered to be a dissipative process. Below, the constitutive description of the dissipative behavior is introduced at the local level of twin interfaces, and then it is upscaled to the macroscopic level by referring to the specific branched microstructure shown in Fig. 1.

In the continuum setting, the twin spacing h is now considered as a function of both position and time, $h = h(x, t)$. Additionally, the length of the twinned domain is time-dependent, such that $0 \leq x \leq L(t)$.

We assume that, at the local level, the dissipative behavior is governed by a local rate-independent dissipation potential (density per unit interface area) that depends on the local interface propagation speed \hat{v}_n (normal to the interface),

$$\hat{D} = \hat{r}|\hat{v}_n|, \quad (24)$$

where \hat{r} is the rate-independent threshold (critical driving force) for interface propagation, and the quantities with a hat refer to the local sharp-interface description. The dependence of the interface speed \hat{v}_n on the rate of change of the twin spacing, \dot{h} , is derived in Appendix A, see Eq. (A.7), and reads

$$\hat{v}_n = \frac{3}{4}(1 - \lambda)\alpha\dot{h}. \quad (25)$$

Referring to the discrete setting, the total dissipation potential $D^{(i)}$ (density per unit volume) for a single cell, see Fig. 1(b), is obtained by averaging over the cell volume. Considering that within the cell there are four interfaces of the length L_i/α (for $L_i \gg h_i$) and assuming that the interface speed \hat{v}_n is identical for all interfaces, we have

$$D^{(i)} = \frac{1}{2h_i L_i} \frac{4L_i}{\alpha} \hat{D} = \frac{2\hat{D}}{\alpha h_i}, \quad (26)$$

and in the continuum setting

$$D = \frac{2\hat{D}}{\alpha h}. \quad (27)$$

Combining Eqs. (24), (25), and (27), the overall dissipation potential is finally obtained in the following form,

$$D = \frac{r}{h} |\dot{h}|, \quad r = \frac{3}{2}(1 - \lambda)\hat{r}. \quad (28)$$

We note that D depends on $|\dot{h}|$ just like \hat{D} depends on $|v_n|$, hence the structure of the dissipation potential is preserved, while the effective threshold is equal to r/h and is inversely proportional to h .

4.2. Evolution problem

Consider now the evolution problem in which the length $L = L(t)$ of the twinned domain is prescribed as a function of time, where $L(t)$ plays the role of a control parameter. To determine the rate of change of the twin spacing, \dot{h} , we formulate a minimization problem for the rate potential Π ,

$$\Pi = \dot{\Phi} + \mathcal{D} \rightarrow \min_{\dot{h}}, \quad (29)$$

where $\dot{\Phi}$ is the rate of change of the total free energy,

$$\dot{\Phi} = \int_0^L \left(Ah_{,x} \dot{h}_{,x} - \frac{2\gamma}{\alpha h^2} \dot{h} \right) dx + \Gamma \dot{h}|_{x=L} + \dot{L}\phi|_{x=L}, \quad (30)$$

and \mathcal{D} is the total dissipation potential,

$$\mathcal{D} = \int_0^L D dx. \quad (31)$$

The necessary condition for the minimum of Π reads

$$0 \in \int_0^L \left(Ah_{,x} \delta \dot{h}_{,x} - \frac{2\gamma}{\alpha h^2} \delta \dot{h} + \partial_{\dot{h}} |\dot{h}| \frac{r}{h} \delta \dot{h} \right) dx + \Gamma \delta \dot{h}|_{x=L} \quad \forall \delta \dot{h}, \quad (32)$$

where the subdifferential $\partial_{\dot{h}} |\dot{h}|$ and the resulting inclusion are introduced in view of non-differentiability of the dissipation potential. Due to the non-smoothness, a direct computational treatment of the above minimization problem is not immediate, and the augmented Lagrangian method (Alart and Curnier, 1991) is used for that purpose. The details are provided in Appendix B.

The dimensionless form of the weak form (32) reads

$$0 \in \int_0^1 \left(\bar{h}_{,\bar{x}} \delta \bar{h}_{,\bar{x}} - \frac{2\bar{\gamma}}{\bar{h}^2} \delta \bar{h} + \partial_{\dot{\bar{h}}} |\dot{\bar{h}}| \frac{\bar{r}}{\bar{h}} \delta \bar{h} \right) d\bar{x} + \bar{\Gamma} \delta \bar{h}|_{\bar{x}=1} \quad \forall \delta \bar{h}, \quad (33)$$

where \bar{r}/\bar{h} is the dimensionless threshold for interface propagation with

$$\bar{r} = \frac{r}{A} = \frac{3(1 - \lambda)\hat{r}}{2A}, \quad (34)$$

and $\delta \bar{h}$ is the test function replacing $\delta \dot{h}$ in the weak form (32). Note also that $\dot{\bar{h}}$ denotes the rate of the dimensionless twin spacing \bar{h} evaluated at a constant x (rather than at a constant \bar{x}). Considering that the domain $(0, L)$ evolves in time, the actual computations are carried out on a fixed domain, $0 \leq \bar{x} \leq 1$, and on a fixed finite-element mesh. This simplifies enforcement of the boundary condition at $x = L$ ($\bar{x} = 1$), but requires a proper computation of the rate of twin spacing. This is discussed further in Appendix B.

4.3. Model predictions

The effect of energy dissipation on the evolution of twin spacing h in the branched microstructure is studied in this section. We consider the scenario in which the length of the twinned domain L increases from L_0 to L_{\max} , followed by a decrease back to L_0 . We set the initial length as $L_0 = 0.01L_{\max}$. Since the evolution is here rate-independent, the length L is a control parameter and plays the role of a pseudo-time. The initial twin spacing corresponding to $L = L_0$ is determined by minimization of the total free energy, as in Section 3.4.

The evolution problem at hand involves one additional material parameter to be specified, namely the rate-independent threshold \hat{r} , see Eq. (24). The remaining parameters are the same as in the study in Section 3.4. The rate-independent threshold is expected to strongly depend on the material, its state (purity, defects, etc.), and on the twinning mode (e.g., type I or type II twinning). To estimate the range of physically-relevant values of \hat{r} , we consider the work of Novak et al. (2006) who performed a comprehensive study on martensite variant reorientation in prism-shaped single crystal of CuAlNi alloy. In the experiment, one variant of martensite is transformed to another variant by compressing the specimen along a specified direction. The transformation proceeds through the evolution of a simple laminate composed of the two variants. Using the respective stress-strain curve, the critical driving force for transformation, which at the microscale corresponds to the rate-independent threshold for interface propagation, can be determined. Accordingly, we have $\hat{r} = \sigma^{\text{tw}} \varepsilon^{\text{tw}}$, where σ^{tw} and ε^{tw} denote the uniaxial transformation (twinning) stress and strain, respectively. It follows that, for type II twinning, the parameter \hat{r} is within the range between 1.25 MPa ($\sigma^{\text{tw}} = 25$ MPa, $\varepsilon^{\text{tw}} = 0.05$, see Fig. 3b in Novak et al. (2006)) and 4 MPa ($\sigma^{\text{tw}} = 130$ MPa, $\varepsilon^{\text{tw}} = 0.033$, see Fig. 3c in Novak et al. (2006)). For compound twins, the threshold is much lower, $\hat{r} \approx 0.03$ MPa ($\sigma^{\text{tw}} \approx 1$ MPa, $\varepsilon^{\text{tw}} = 0.03$, see the V2→V1 transformation in Fig. 2b in Novak et al. (2006)). Finally, it is worthwhile to note that type I twins have not been observed in their study. In the following analysis, we will use a relatively high value of $\hat{r} = 4$ MPa, as determined above, so that the effects of energy dissipation are well visible. According to Eq. (34), the corresponding dimensionless parameter is here $\bar{r} = 0.21$.

For the purpose of presentation of the results, it is convenient to introduce an alternative normalization based on the maximum length L_{\max} , rather than on the current length L as in Eqs. 17, 19, and (20). The corresponding dimensionless quantities are denoted by a superimposed tilde, namely

$$\tilde{h} = \frac{h}{L_{\max}}, \quad \tilde{x} = \frac{x}{L_{\max}}, \quad \tilde{L} = \frac{L}{L_{\max}}, \quad \tilde{\gamma} = \frac{\gamma}{\alpha A L_{\max}}, \quad \tilde{\Phi} = \frac{\Phi}{A L_{\max}}. \quad (35)$$

Sample results are presented in Fig. 5 for $L_{\max} = 20 \mu\text{m}$ which corresponds to $\tilde{\gamma} = 10^{-3}$ for the adopted material parameters. The evolution of twin spacing \tilde{h} is shown in Fig. 5(a,b) where the individual curves correspond to selected values of the domain length \tilde{L} . As a reference, the dashed lines show the corresponding profiles of twin spacing obtained by minimization of the total free energy (no dissipation, $\hat{r} = 0$). In the first stage of the evolution, when the domain length L increases, Fig. 5(a), the twin spacing increases, however, the increase is slowed down as compared to the case with no dissipation. In the second stage, when the domain length L decreases, Fig. 5(b), the evolution is more complex. Initially, there is a zone in which the twin spacing does not evolve.

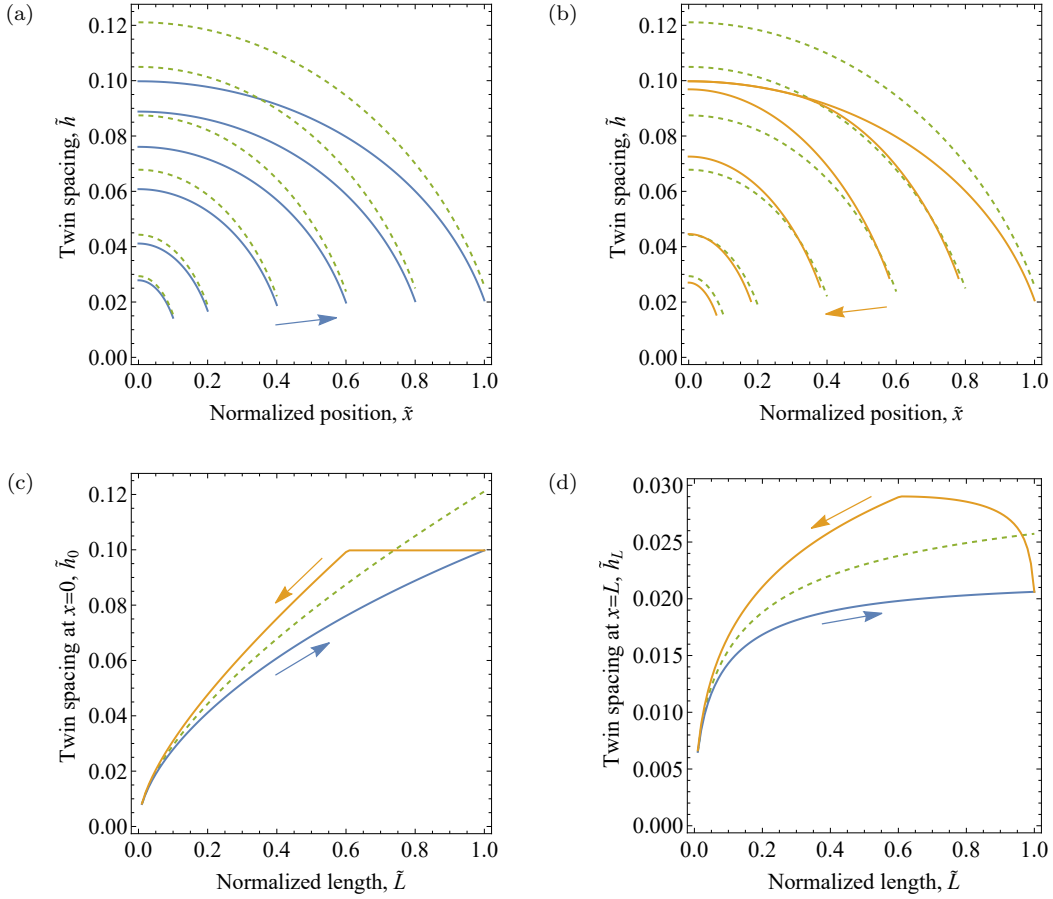


Figure 5: Evolution of twin spacing \tilde{h} for $\tilde{\gamma} = 10^{-3}$ ($L_{\max} = 20 \mu\text{m}$) and $\bar{r} = 0.21$ ($\hat{r} = 4 \text{ MPa}$): (a,b) \tilde{h} as a function of \tilde{x} while \tilde{L} is increasing (a) and decreasing (b); (c,d) twin spacing at $x = 0$ (c) and at $x = L$ (d) as a function of the domain length \tilde{L} . The dashed lines correspond to the case with no dissipation, $\hat{r} = 0$.

This, in particular, concerns the free end, at $x = 0$, see Fig. 5(c). The evolution of the twin spacing at the other end of the domain, at $x = L$, is shown in Fig. 5(d).

Fig. 6 shows the evolution of the total free energy $\tilde{\Phi}$ and its contributions defined in Eq. (23). While the effect of energy dissipation on the individual contributions is significant, see Fig. 6(b,c,d), the total energy is only marginally affected and is very close to the case of no dissipation (depicted by the dashed line), see Fig. 6(a). Clearly, in the dissipative case, the total free energy is higher than in the case with no dissipation, since the later case corresponds to the minimum of the total free energy.

To investigate the effect of energy dissipation further, two other cases are considered and reported in Figs. 7 and 8. Specifically, the maximum domain length L_{\max} is decreased and increased 10 times with respect to the previous example, while all the remaining parameters remain unchanged. The case of $L_{\max} = 2 \mu\text{m}$, which corresponds to $\tilde{\gamma} = 10^{-2}$, is shown in Fig. 7. It can be seen that the effect of dissipation on the evolution of twin spacing is more pronounced than for $\tilde{\gamma} = 10^{-3}$ shown in Fig. 5. Similarly, the effect on the total free energy $\tilde{\Phi}$ is also more pronounced, see Fig. 7(c). On the other hand, for $L_{\max} = 200 \mu\text{m}$, which corresponds to $\tilde{\gamma} = 10^{-4}$, the effect of energy dissipation

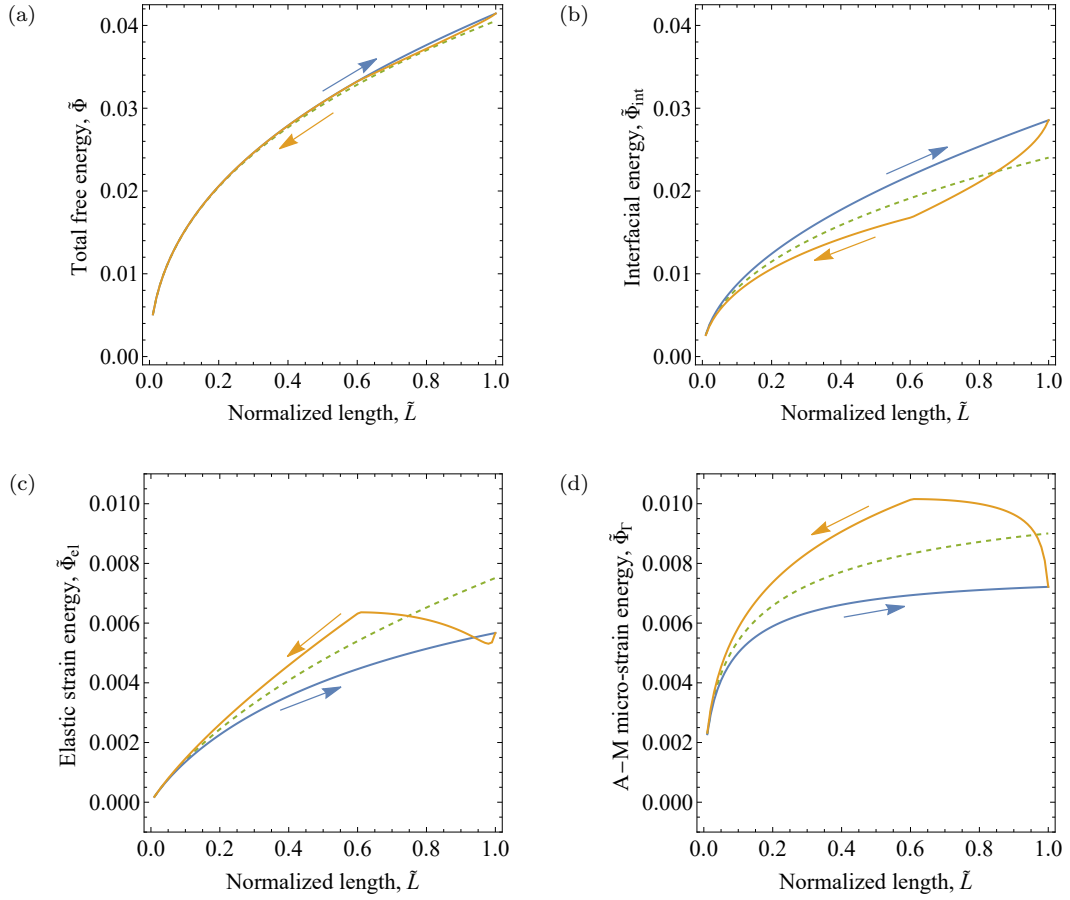


Figure 6: Evolution of the total free energy $\bar{\Phi}$ and individual energy contributions $\bar{\Phi}_{\text{int}}$, $\bar{\Phi}_{\text{el}}$, $\bar{\Phi}_{\Gamma}$ for $\bar{\gamma} = 10^{-3}$ ($L_{\text{max}} = 20 \mu\text{m}$) and $\bar{r} = 0.21$ ($\hat{r} = 4 \text{ MPa}$). The dashed lines correspond to the case with no dissipation, $\hat{r} = 0$.

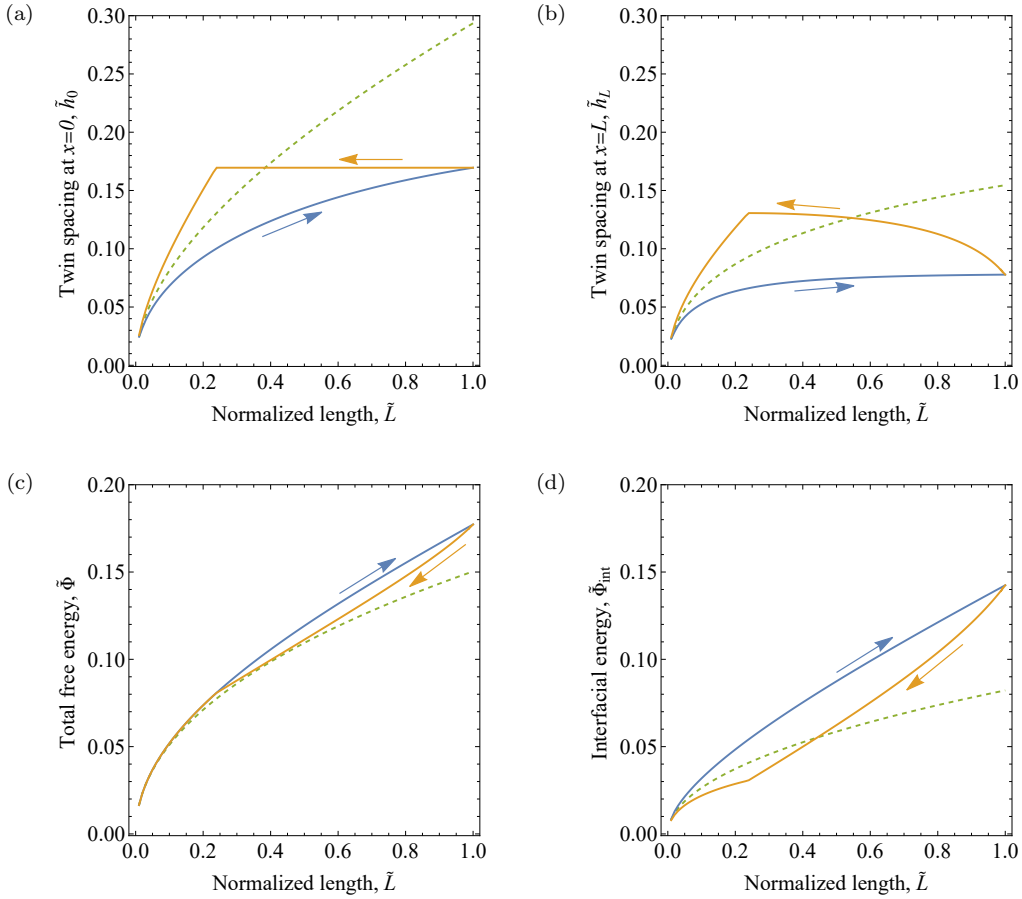


Figure 7: Evolution of the twin spacing \tilde{h} at $x=0$ (a) and at $x=L$ (b), total free energy $\tilde{\Phi}$ (c) and its interfacial contribution $\tilde{\Phi}_{\text{int}}$ (d) for $\tilde{\gamma} = 10^{-2}$ ($L_{\text{max}} = 2 \mu\text{m}$) and $\tilde{r} = 0.21$ ($\hat{r} = 4 \text{ MPa}$). The dashed lines correspond to the case with no dissipation, $\hat{r} = 0$.

on the twin spacing is visible, but small, while the effect on the total free energy is negligible, see Fig. 8.

The results presented above, Figs. 5–8, correspond to a relatively large value of the rate-independent threshold ($\hat{r} = 4 \text{ MPa}$) and to relatively small domain sizes (L_{max} varied between 2 and $200 \mu\text{m}$ so that $\tilde{\gamma}$ varies between 10^{-2} and 10^{-4} , respectively). For these parameters, the effect of energy dissipation on the evolution of branched microstructure, as characterized by the twin spacing, is visible, while the effect on the total free energy is limited (the effect is more pronounced for the individual energy contributions). For larger domain sizes L_{max} (i.e., for smaller values of the dimensionless twin boundary energy $\tilde{\gamma}$), the respective effects are smaller and can be considered insignificant. Of course, the effects of energy dissipation are also weaker for smaller values of the rate-independent threshold \hat{r} . For instance, when the case of $\tilde{\gamma} = 10^{-2}$ is considered, as in Fig. 7, but parameter \hat{r} is reduced twice (to 2 MPa), the effect of energy dissipation is qualitatively similar (although somewhat more pronounced) as in the case of $\tilde{\gamma} = 10^{-3}$ and $\hat{r} = 4 \text{ MPa}$, see Figs. 5 and 6. The corresponding results are not shown for brevity.

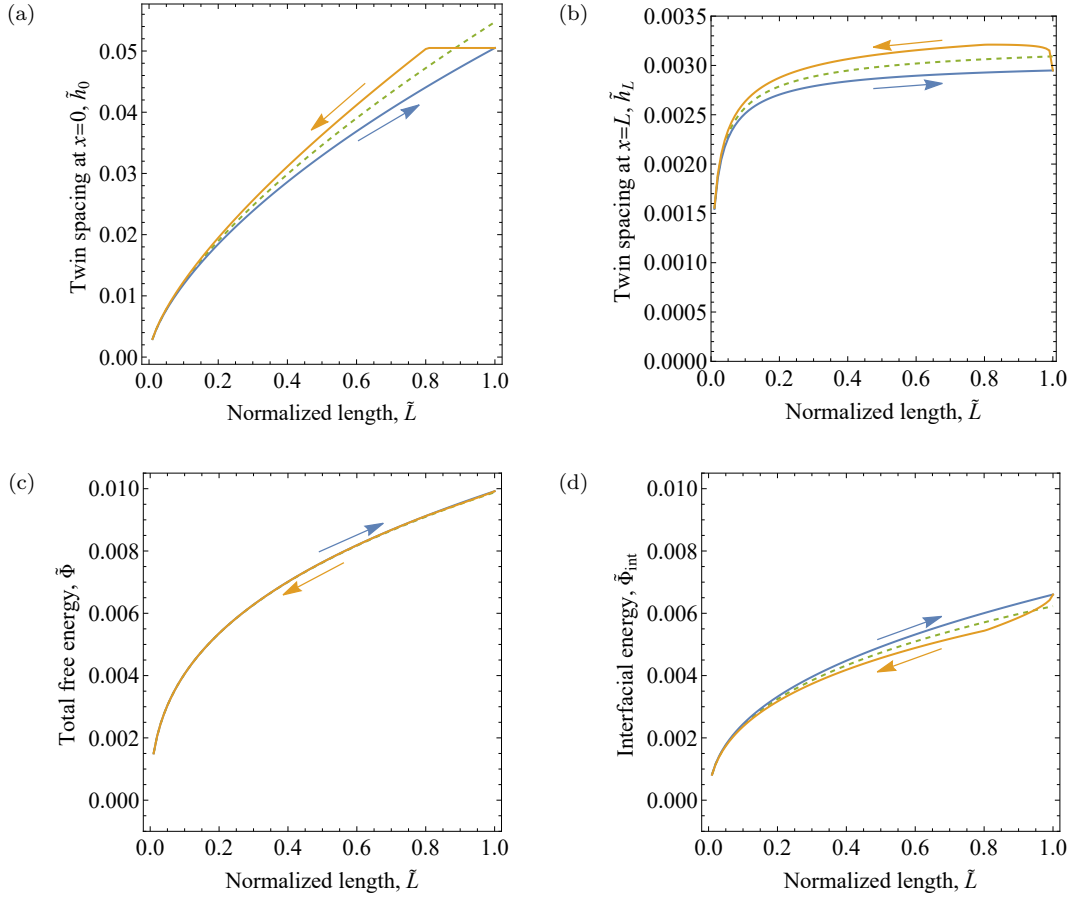


Figure 8: Evolution of the twin spacing \bar{h} at $x = 0$ (a) and at $x = L$ (b), total free energy $\bar{\Phi}$ (c) and its interfacial contribution $\bar{\Phi}_{\text{int}}$ (d) for $\bar{\gamma} = 10^{-4}$ ($L_{\text{max}} = 200 \mu\text{m}$) and $\bar{\tau} = 0.21$ ($\hat{r} = 4 \text{ MPa}$). The dashed lines correspond to the case with no dissipation, $\hat{r} = 0$.

5. Discussion

Following Seiner et al. (2020), the specific model discussed above corresponds to the situation in which the twinned domain is bounded by the A–MM interface on its one end and by a free surface on the other end. This is a special case that may be encountered in a single crystal undergoing martensitic transformation. A different situation is expected in the case of a twinned martensite plate formed within a grain in a polycrystalline material. One possible scenario would be that the twinned martensite plate is bounded by two A–MM interfaces (no free surfaces). The proposed approach is directly applicable in such a case as well. It suffices to consider the domain $x \in [-L, L]$ with an adequate boundary condition at $x = -L$, namely $h_{,x}|_{x=-L} = \bar{\Gamma}/A$, cf. Eq. (16)₂. Indeed, the corresponding solution can be obtained directly from the solution obtained for the original problem formulated in Section 3.2 by simply exploiting the symmetry with respect to $x = 0$ (note the homogeneous natural boundary condition at $x = 0$, Eq. (16)₁).

An analogous extension of the problem in the case of evolution with dissipation effects would be possible only when the martensite plate grows and shrinks in a symmetric manner. Other situations, for instance, propagation of only one A–MM interface while the other one is halted, would require revision of the relationship between the rate of twin spacing and the local interface speed, see Eq. (25). Finally, several more complex situations may be encountered when twinned martensite domain terminates at other types of (macroscopic) interfaces, for instance, at the interface between two twinned domains or at the interface between twinned martensite and a single variant of martensite. Each case would require separate modeling assumptions.

It has been shown in Section 3 that the problem of minimization of the total free energy (no dissipation) is fully characterized by two dimensionless parameters, $\bar{\gamma}$ and $\bar{\Gamma}$, see Eqs. (18) and (19). The results reported in Fig. 3 demonstrate that, over a wide range of values of the parameter $\bar{\gamma}$ (say, for $\bar{\gamma} < 10^{-3}$), the dimensionless total energy $\bar{\Phi}$ and twin spacing \bar{h}_0 at $x = 0$ are practically insensitive to $\bar{\Gamma}$ and hence depend solely on $\bar{\gamma}$. This regime corresponds to a significant activity of branching so that the twin spacing at the A–MM interface, \bar{h}_L , is much smaller than that at the free boundary, \bar{h}_0 . Note, however, that the respective contribution to the total free energy, $\bar{\Phi}_\Gamma = \bar{\Gamma}\bar{h}_L$, is then small, but not negligible, see Fig. 4(b). Note also that, although $\bar{\Phi}$ and \bar{h}_0 are not sensitive to $\bar{\Gamma}$ in this regime, the twin spacing \bar{h}_L is visibly affected by $\bar{\Gamma}$, and so is the number of branching generations, N , see Fig. 3(c,d).

Given that the grain size in a polycrystalline aggregate typically ranges from $1\ \mu\text{m}$ to $100\ \mu\text{m}$, the regime of small $\bar{\gamma}$ (equivalent to large L) is less relevant for microstructures developing in polycrystals. This is because L , which is bounded by the grain size, is then small (which corresponds to the regime of large $\bar{\gamma}$). Consequently, twin branching is less likely to occur in polycrystalline materials or is then less pronounced. However, this characterization is relative and also depends on specific material properties.

It is important to remark that there is quite some uncertainty concerning the values of the material parameters, particularly, the twin boundary energy γ and the rate-independent interface propagation threshold \hat{r} . Also the value of parameter A characterizing the elastic strain energy of branching has been determined using the upper bound estimate provided by Seiner et al. (2020). To allow direct comparison with the predictions of the model of Seiner et al. (2020), we have used the estimate corresponding to isotopic elastic properties, Eq. (4). On the other hand, it is well

known that the CuAlNi alloy is elastically highly anisotropic (Sedláč et al., 2005), hence accounting for the elastic anisotropy may influence the value of A (the corresponding estimate has also been provided by Seiner et al. (2020)). In any case, the actual accuracy of those estimates is not known. Alternative estimates, for instance, from direct simulations of branched microstructures, are not available.

In the model of the evolution of the branched microstructure, we have assumed that dissipation is rate-independent. It is generally accepted that rate-independent dissipation is a relevant choice for shape memory alloys, at least, at higher spatial and temporal scales (Petryk and Stupkiewicz, 2010). Concerning the rate-independent threshold \hat{r} , we have estimated a physically relevant range of its values using the experiments of Novak et al. (2006). The availability of these estimates is actually another reason to adopt the rate-independent dissipation model. We have additionally developed a version of the model employing viscous dissipation, with the dissipation potential being quadratic in the interface speed \hat{v}_n . We have verified that the viscous model can deliver results qualitatively similar to those of the rate-independent model. This is achieved by appropriately adjusting the interface mobility parameter (and/or the rate of change of the domain size L). Nevertheless, we do not report these results due to the lack of experimental evidence supporting a physically relevant value for interface mobility.

6. Conclusion

A new approach to the modeling of twin branching in shape memory alloys has been developed in which twin spacing is treated as a continuous function of the distance from the austenite–martensite interface. The free energy, which comprises the interfacial and elastic strain contributions, is then expressed in terms of the twin spacing and its gradient. The total free energy is minimized, and the problem is solved numerically using the finite element method. The resulting 1D model can be considered a continuum counterpart of the discrete model of Seiner et al. (2020), and a very good agreement between the two models has been demonstrated within the entire range of physically relevant model parameters.

The dimensionless formulation of the model, which in the continuum setting is introduced in a natural way, indicates that the problem is fully characterized by two dimensionless parameters expressed in terms of the material properties and of the size of the twinned domain. The results show that, in a wide range of values of the dimensionless interfacial energy $\bar{\gamma}$, the solution is practically insensitive to parameter $\bar{\Gamma}$ characterizing the energy of elastic micro-strains at the A–MM interface. In this regime, the problem is thus fully characterized by only one dimensionless parameter, $\bar{\gamma}$.

The evolution of the branched microstructure has also been studied by considering the energy dissipation associated with propagation of the twin interfaces. The evolution is governed by a minimization problem formulated for a rate potential comprising the free energy rate and the dissipation potential. The results show that, for a high but realistic rate-independent threshold for interface propagation, the energy dissipation effects are significant only for high values of the dimensionless interfacial energy parameter $\bar{\gamma}$ (for instance, for a relatively small size of the twinned domain). Otherwise, the energy dissipation effects are negligible so that effectively the problem is history independent and minimization of the free energy alone suffices to determine the twin spacing and other characteristics. Interestingly, the twin spacing and the individual contributions

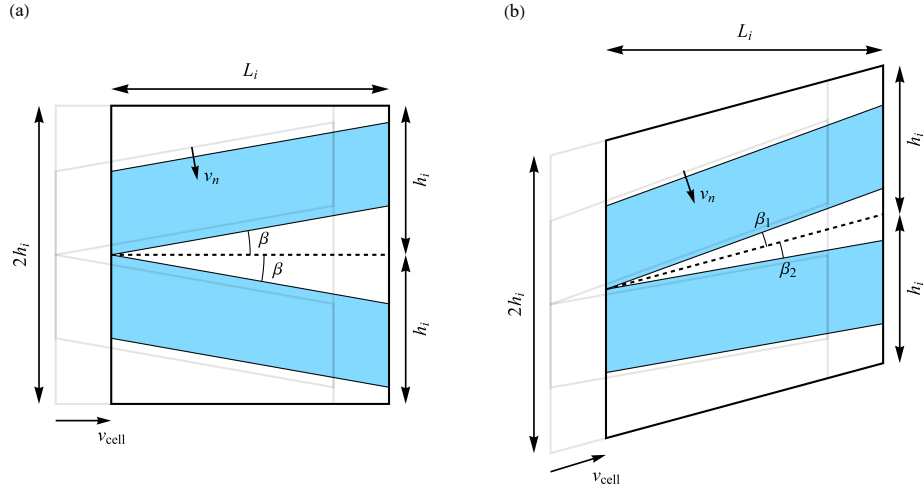


Figure A.1: Estimating the local interface propagation speed \hat{v}_n : (a) $\alpha = 1$; (b) $\alpha \neq 1$. The location of the cell at an earlier instant is indicated in gray.

to the total free energy exhibit a visibly higher sensitivity to the dissipation effects than the total free energy itself.

To the best of our knowledge, this is the first time that the energy dissipation effects are included in the modeling of twin branching phenomena. This has been facilitated by the continuum description adopted in this work, as otherwise modeling of an evolution problem would be difficult, if possible at all.

Acknowledgments. This work has been partially supported by the National Science Centre (NCN) in Poland through the Grant No. 2021/43/D/ST8/02555. For the purpose of Open Access, the authors have applied a CC-BY public copyright license to any Author Accepted Manuscript (AAM) version arising from this submission.

Appendix A. Estimation of local interface propagation speed

In this appendix, an estimate of the local interface propagation speed \hat{v}_n is derived as a function of \dot{h} , the rate of change of the twin spacing. Referring to the discrete model of branching shown in Fig. 1, we assume that locally the evolution of the branched microstructure, i.e., the change of the twin spacing, proceeds by a ‘rigid’ translation of the cells, see Fig. A.1. For the purpose of estimating the relationship between the propagation speed of individual interfaces and the rate of change of the twin spacing, we thus neglect the possible change of the proportions of the cells.

The derivation is first performed for a simplified case when the (nominal) twin interfaces are perpendicular to the A–MM interface, thus $\mathbf{m} \cdot \mathbf{n} = 0$ and $\alpha = 1$, see Eq. (5)₁. Consider thus a rigid translation of the unit cell with the speed v_{cell} , as shown in Fig. A.1(a). The resulting interface propagation speed \hat{v}_n (measured in the direction normal to the local twin interfaces) is thus given by

$$\hat{v}_n = v_{\text{cell}} \sin \beta \approx v_{\text{cell}} \tan \beta. \quad (\text{A.1})$$

Here and below, we assume that $L_i \gg h_i$ which implies that the angle β is small. From the geometry of the unit cell, we have

$$\tan \beta = \frac{(1-\lambda)h_i}{2} \frac{1}{L_i} = -\frac{3}{4}(1-\lambda)h_{,x} \quad (\text{for } \alpha = 1), \quad (\text{A.2})$$

where Eq. (8) has also been used.

In line with the assumption of rigid translation of the unit cell, the ‘material time derivative’ of the twin spacing $h = h(x, t)$ vanishes so that

$$\frac{Dh}{Dt} = \frac{\partial h}{\partial t} + \frac{\partial h}{\partial x} \frac{\partial x}{\partial t} = \dot{h} + h_{,x} v_{\text{cell}} = 0, \quad v_{\text{cell}} = -\frac{\dot{h}}{h_{,x}} \quad (\text{for } \alpha = 1). \quad (\text{A.3})$$

Combining Eqs. (A.1)–(A.3), the interface speed \hat{v}_n can now be expressed as a function of \dot{h} ,

$$\hat{v}_n = \frac{3}{4}(1-\lambda)\dot{h} \quad (\text{for } \alpha = 1). \quad (\text{A.4})$$

Let us now consider the general case of $\mathbf{m} \cdot \mathbf{n} \neq 0$ and $\alpha \neq 1$, see Fig. A.1(b). The unit cell is no longer symmetric. This in particular implies that angles β_1 and β_2 are not equal. However, in view of $L_i \gg h_i$, we neglect this (small) difference, and the counterpart of Eq. (A.2) reads

$$\beta_1 \approx \beta_2 = \beta, \quad \tan \beta = \frac{(1-\lambda)\alpha h_i}{2} \frac{\alpha}{L_i} = -\frac{3}{4}(1-\lambda)\alpha^2 h_{,x}. \quad (\text{A.5})$$

This also implies that the propagation speed \hat{v}_n is equal for all interfaces and that Eq. (A.1) holds.

Considering that the rigid translation of the unit cell is directed along the nominal twin interfaces, the ‘advection’ speed in Eq. (A.3) is now equal to αv_{cell} so that the counterpart of Eq. (A.3) takes the form

$$\frac{Dh}{Dt} = \dot{h} + h_{,x} \alpha v_{\text{cell}} = 0, \quad v_{\text{cell}} = -\frac{\dot{h}}{\alpha h_{,x}}. \quad (\text{A.6})$$

By combining Eqs. (A.1), (A.5) and (A.6) the dependence of the interface speed \hat{v}_n on the rate of change of the twin spacing, \dot{h} , is finally found in the following form,

$$\hat{v}_n = \frac{3}{4}(1-\lambda)\alpha\dot{h}. \quad (\text{A.7})$$

Refined estimates could be derived by considering the actual geometry in more detail. The simple estimate derived above is sufficient for the present purpose, as it shows the structure of the dependence of \hat{v}_n on \dot{h} .

Appendix B. Computational treatment of the evolution problem

The minimization problem (29) is non-smooth, and its computational treatment relies on the augmented Lagrangian technique Alart and Curnier (1991), borrowed here from computational contact mechanics. An equivalent smooth saddle-point problem is thus formulated,

$$L = \dot{\Phi} + \mathcal{L} \rightarrow \min_h \max_\lambda, \quad (\text{B.1})$$

where λ is the Lagrange multiplier field that is introduced through the functional \mathcal{L} ,

$$\mathcal{L} = \int_0^L \frac{r}{h} l(\dot{h}, \lambda) dx. \quad (\text{B.2})$$

The function $l(\dot{h}, \lambda)$ is defined as

$$l(\dot{h}, \lambda) = \begin{cases} \left(\lambda + \frac{1}{2}\varrho\dot{h}\right)\dot{h} & \text{if } |\hat{\lambda}| \leq 1, \\ -\frac{1}{2\varrho}\left(\lambda^2 - 2|\hat{\lambda}| + 1\right) & \text{if } |\hat{\lambda}| > 1, \end{cases} \quad (\text{B.3})$$

where $\hat{\lambda} = \lambda + \varrho\dot{h}$ is the augmented Lagrange multiplier, and $\varrho > 0$ is a positive constant.

The Lagrange functional L is smooth (because function $l(\dot{h}, \lambda)$ is continuously differentiable) hence the solution of the saddle-point problem (B.1) can be found by solving the condition of stationarity of L with respect to arbitrary variations of \dot{h} and λ , which reads

$$\int_0^L \left(Ah_{,x} \delta \dot{h}_{,x} - \frac{2\gamma}{\alpha h^2} \delta \dot{h} + \frac{r}{h} \hat{\lambda}_{\text{eff}} \delta \dot{h} \right) dx + \Gamma \delta \dot{h} \Big|_{x=L} = 0 \quad \forall \delta \dot{h}, \quad (\text{B.4})$$

$$\int_0^L \frac{r}{h} C_{\text{eff}} \delta \lambda dx = 0 \quad \forall \delta \lambda, \quad (\text{B.5})$$

where

$$\hat{\lambda}_{\text{eff}} = \frac{\partial l}{\partial \dot{h}} = \begin{cases} \hat{\lambda} & \text{if } |\hat{\lambda}| \leq 1, \\ \text{sign } \hat{\lambda} & \text{if } |\hat{\lambda}| > 1, \end{cases} \quad C_{\text{eff}} = \frac{\partial l}{\partial \lambda} = \begin{cases} \dot{h} & \text{if } |\hat{\lambda}| \leq 1, \\ -\frac{1}{\varrho}(\lambda - \text{sign } \hat{\lambda}) & \text{if } |\hat{\lambda}| > 1. \end{cases} \quad (\text{B.6})$$

Eq. (B.4) is a continuous counterpart of Eq. (32) with the effective Lagrange multiplier $\hat{\lambda}_{\text{eff}}$ replacing the subdifferential $\partial_{\dot{h}}|\dot{h}|$. On the other hand, Eq. (B.5) is a weak form of a state-dependent constraint $C_{\text{eff}} = 0$ which enforces $\dot{h} = 0$ when $|\hat{\lambda}| \leq 1$ and $\lambda = \text{sign } \hat{\lambda} = \pm 1$ when $|\hat{\lambda}| > 1$. Note that the augmented Lagrangian method delivers a numerically exact solution that is independent of the value of parameter ϱ .

At each time increment, the saddle-point problem specified above is solved using the finite element method. Recall that to facilitate enforcement of the natural boundary condition at $x = L$, see Eq. (16)₂, the computations are carried out in a dimensionless form on a fixed domain $0 \leq \bar{x} \leq 1$ (and on a fixed mesh). Applying the backward-Euler time integration scheme, the dimensionless form of Eqs. (B.4) and (B.5) reads

$$\int_0^1 \left(\bar{h}_{,\bar{x}} \delta \bar{h}_{,\bar{x}} - \frac{2\bar{\gamma}}{\bar{h}^2} \delta \bar{h} + \frac{\bar{r}}{\bar{h}} \bar{\lambda}_{\text{eff}} \delta \bar{h} \right) d\bar{x} + \bar{\Gamma} \delta \bar{h} \Big|_{\bar{x}=1} = 0 \quad \forall \delta \bar{h}, \quad (\text{B.7})$$

$$\int_0^1 \frac{\bar{r}}{\bar{h}} \bar{C}_{\text{eff}} \delta \lambda d\bar{x} = 0 \quad \forall \delta \lambda, \quad (\text{B.8})$$

where

$$\bar{\lambda}_{\text{eff}} = \begin{cases} \bar{\lambda} & \text{if } |\bar{\lambda}| \leq 1, \\ \text{sign } \bar{\lambda} & \text{if } |\bar{\lambda}| > 1, \end{cases} \quad \bar{C}_{\text{eff}} = \begin{cases} \Delta \bar{h} & \text{if } |\bar{\lambda}| \leq 1, \\ -\frac{1}{\bar{\varrho}}(\lambda - \text{sign } \bar{\lambda}) & \text{if } |\bar{\lambda}| > 1, \end{cases} \quad (\text{B.9})$$

$\bar{\lambda} = \lambda + \bar{\varrho}\Delta\bar{h}$ and $\bar{\varrho} = L\varrho$. Note that the problem is rate-independent, hence, upon time discretization, the rate \dot{h} is here approximated directly by the increment $\Delta h = h_{n+1} - h_n$ without specifying the corresponding time increment.

As already discussed in Section 4.2, in the dimensionless setting, the rate (or increment) of the twin spacing must be evaluated at a fixed coordinate x . Accordingly, at each point $\bar{x} = x/L_{n+1}$, the increment $\Delta\bar{h}$ is defined as

$$\Delta\bar{h}(\bar{x}) = \frac{h_{n+1}(x) - h_n^{\text{ext}}(x)}{L_{n+1}} = \bar{h}_{n+1}(\bar{x}) - \frac{L_n}{L_{n+1}} \bar{h}_n^{\text{ext}}(\bar{x}_n^*), \quad \bar{x}_n^* = \frac{L_{n+1}}{L_n} \bar{x}, \quad (\text{B.10})$$

where \bar{x}_n^* is the dimensionless position of the point $x = \bar{x}L_{n+1}$ at the previous time step and

$$\bar{h}_n^{\text{ext}}(\bar{x}) = \begin{cases} \bar{h}_n(\bar{x}) & \text{if } 0 \leq \bar{x} \leq 1, \\ 0 & \text{if } \bar{x} > 1. \end{cases} \quad (\text{B.11})$$

Here, \bar{h}_n^{ext} is an extension of \bar{h}_n defined also for $\bar{x} > 1$, which is needed to compute $\Delta\bar{h}$ when $L_{n+1} > L_n$. The above simple treatment is sufficient because, in the case of rate-independent dissipation, only the sign of the increment $\Delta\bar{h}$ enters the actual governing equations.

The weak forms (B.7) and (B.8) constitute the basis for the finite-element implementation of the model. The Lagrange multipliers λ are introduced as additional global unknowns, otherwise the implementation follows a standard procedure, as briefly described in Section 3.3.

References

- Alart, P., Curnier, A., 1991. A mixed formulation for frictional contact problems prone to Newton like solution methods. *Comput. Methods Appl. Mech. Eng.* 92, 353–375.
- Amini, S., Rezaee-Hajidehi, M., Stupkiewicz, S., 2023. Energy and morphology of martensite-twinning interface in CuAlNi shape memory alloy: A phase-field study. *Comp. Mater. Sci.* 230, 112472.
- Ball, J.M., James, R.D., 1987. Fine phase mixtures as minimizers of energy. *Arch. Ration. Mech. Anal.* 100, 13–52.
- Bhattacharya, K., 2003. *Microstructure of martensite: why it forms and how it gives rise to the shape-memory effect.* Oxford University Press, Oxford.
- Bronstein, E., Faran, E., Shilo, D., 2019. Analysis of austenite-martensite phase boundary and twinned microstructure in shape memory alloys: The role of twinning disconnections. *Acta Mater.* 164, 520–529.
- Capella, A., Otto, F., 2009. A rigidity result for a perturbation of the geometrically linear three-well problem. *Commun. Pure Appl. Math.* 62, 1632–1669.
- Chan, A., Conti, S., 2015. Energy scaling and branched microstructures in a model for shape-memory alloys with $SO(2)$ invariance. *Math. Models Methods Appl. Sci.* 25, 1091–1124.
- Chu, C., 1993. *Hysteresis and microstructures: a study of biaxial loading on compound twins of copper-aluminum-nickel single crystals.* Ph.D. thesis. University of Minnesota.
- Conti, S., 2000. Branched microstructures: scaling and asymptotic self-similarity. *Commun. Pure Appl. Math.* 53, 1448–1474.
- Dondl, P., Heeren, B., Rumpf, M., 2016. Optimization of the branching pattern in coherent phase transitions. *C. R. Math.* 354, 639–644.
- Finel, A., Le Bouar, Y., Gaubert, A., Salman, U., 2010. Phase field methods: Microstructures, mechanical properties and complexity. *C. R. Physique* 11, 245–256.

- Hubert, A., Schäfer, R., 1998. Magnetic domains: the analysis of magnetic microstructures. Springer Science & Business Media.
- Huebener, R., 2001. Magnetic flux structures in superconductors: extended reprint of a classic text. Springer Science & Business Media.
- Khachaturyan, A.G., 1983. Theory of structural transformation in solids. Wiley, New York.
- Kohn, R.V., Müller, S., 1992. Branching of twins near an austenite—twinned-martensite interface. *Philos. Mag. A* 66, 697–715.
- Kohn, R.V., Müller, S., 1994. Surface energy and microstructure in coherent phase transitions. *Commun. Pure Appl. Math.* 47, 405–435.
- Li, B., Luskin, M., 1999. Theory and computation for the microstructure near the interface between twinned layers and a pure variant of martensite. *Mat. Sci. Engng. A* 273, 237–240.
- Ma, L., He, L., Ni, Y., 2020. Tunable hierarchical wrinkling: From models to applications. *J. Appl. Phys.* 127.
- Maciejewski, G., Stupkiewicz, S., Petryk, H., 2005. Elastic micro-strain energy at the austenite-twinned martensite interface. *Arch. Mech.* 57, 277–297.
- Novak, V., Šittner, P., Ignacová, S., Černoč, T., 2006. Transformation behavior of prism shaped shape memory alloy single crystals. *Mat. Sci. Engng. A* 438, 755–762.
- Petryk, H., Stupkiewicz, S., 2010. Interfacial energy and dissipation in martensitic phase transformations. Part I: Theory. *J. Mech. Phys. Solids* 58, 390–408.
- Petryk, H., Stupkiewicz, S., Maciejewski, G., 2006. Modeling of austenite/martensite laminates with interfacial energy effect, in: *Proceedings of IUTAM Symposium on Size Effects on Material and Structural Behavior at Micron-and Nano-Scales*, Springer. pp. 151–162.
- Petryk, H., Stupkiewicz, S., Maciejewski, G., 2010. Interfacial energy and dissipation in martensitic phase transformations. Part II: Size effects in pseudoelasticity. *J. Mech. Phys. Solids* 58, 373–389.
- Qin, G., Zhang, C., Zhang, S., Chen, X., He, Y., 2023. Compatibility effect on stress-free two-way memory of Ni-Mn-Ga single crystal. *J. Alloys Compd.* 935, 168134.
- Sedlák, P., Seiner, H., Landa, M., Novák, V., Šittner, P., Mañosa, L., 2005. Elastic constants of bcc austenite and 2H orthorhombic martensite in CuAlNi shape memory alloy. *Acta Mater.* 53, 3643–3661.
- Seiner, H., Plucinsky, P., Dabade, V., Benešová, B., James, R.D., 2020. Branching of twins in shape memory alloys revisited. *J. Mech. Phys. Solids* 141, 103961.
- Simon, T., 2021. Rigidity of branching microstructures in shape memory alloys. *Arch. Ration. Mech. Anal.* 241, 1707–1783.
- Stupkiewicz, S., Maciejewski, G., Petryk, H., 2007. Low-energy morphology of the interface layer between austenite and twinned martensite. *Acta Mater.* 55, 6292–6306.

- Tůma, K., Stupkiewicz, S., 2016. Phase-field study of size-dependent morphology of austenite–twinned martensite interface in CuAlNi. *Int. J. Solids Struct.* 97, 89–100.
- Vandeparre, H., Gabriele, S., Brau, F., Gay, C., Parker, K.K., Damman, P., 2010. Hierarchical wrinkling patterns. *J. Soft Matter* 6, 5751–5756.